
Implications of spatial reservoir uncertainty for CO₂ sequestration in the east Snake River Plain, Idaho (USA)

Ryan M. Pollyea · Jerry P. Fairley

Abstract Basalt-hosted hydrogeologic systems have been proposed for geologic CO₂ sequestration based on laboratory research suggesting rapid mineralization rates. However, despite this theoretical appeal, little is known about the impacts of basalt fracture heterogeneity on CO₂ migration at commercial scales. Evaluating the suitability of basalt reservoirs is complicated by incomplete knowledge of in-situ fracture distributions at depths required for CO₂ sequestration. In this work, a numerical experiment is used to investigate the effects of spatial reservoir uncertainty for geologic CO₂ sequestration in the east Snake River Plain, Idaho (USA). Two criteria are investigated: (1) formation injectivity and (2) confinement potential. Several theoretical tools are invoked to develop a field-based approach for geostatistical reservoir characterization and their implementation is illustrated. Geologic CO₂ sequestration is simulated for 10 years of constant-rate injection at ~680,000 tons per year and modeled by Monte Carlo simulation such that model variability is a function of spatial reservoir heterogeneity. Results suggest that the spatial distribution of heterogeneous permeability structures is a controlling influence on formation injectivity. Analysis of confinement potential is less conclusive; however, in the absence of confining sedimentary interbeds within the basalt pile, rapid mineralization may be necessary to reduce the risk of escape.

Keywords Geologic carbon sequestration · Fractured rocks · Geostatistics · Heterogeneity · USA

Introduction

Geologic carbon sequestration has emerged as a promising approach for reducing atmospheric CO₂ emissions from

fossil fuel-based energy production. At the most fundamental level, geologic carbon sequestration is disposal of captured CO₂ by burial in deep geologic formations, the most common of which are depleted oil fields and sedimentary basins (Orr 2009). Within the portfolio of geologic carbon sequestration technologies, perhaps the least understood and investigated is carbon disposal in deep basalt-hosted hydrogeologic systems. Basalt formations are geographically attractive for geologic carbon sequestration due to the regionally expansive basalt provinces of the northwestern United States and rapidly growing population centers in western India, where CO₂ storage estimates of 100 and 150 gigatons, respectively, have been suggested (McGrail et al. 2006; Jayaraman 2007).

Geologic carbon sequestration in basalt aquifers is based on the premise that CO₂ injected at target depths, typically greater than 800 m, may induce a series of calcium/magnesium dissolution reactions in the host rock followed by calcite precipitation, the result of which is long-term CO₂ disposal by permanent mineral trapping (McGrail et al. 2006; Schaef and McGrail 2009; Matter and Kelemen 2009; Prasad et al. 2009). These reactions have been shown to be kinetically favorable, and it has been suggested that calcite precipitation may be induced on a time scale of 10²–10³ days (McGrail et al. 2006, their Table 2). However, despite this theoretical appeal of CO₂ trapping by mineralization, there exists a great deal of uncertainty with respect to reservoir-scale implementation. Several reservoir characteristics have been proposed for evaluating the reservoir suitability of carbon sequestration in any geologic formation; these include capacity, injectivity, and confinement (Bachu 2008). In a general sense, capacity is the reservoir storage potential (mass CO₂), injectivity is the ability of the formation to accept the injected CO₂, and confinement is the ability of the formation to prevent vertical migration, i.e. escape, of injected CO₂. Within fractured basalt formations, the injectivity and confinement are of particular concern due to a paradox inherent to carbon disposal in fractured rocks: densely fractured basalt flow margins represent the primary conduits for CO₂ transport and storage and the connectivity of these features is necessary for maintaining sufficiently low injection pressures. Conversely, too much connectivity has the adverse effect of increasing the likelihood of CO₂ escaping the target reservoir. One

Received: 9 September 2011 / Accepted: 13 March 2012
Published online: 4 April 2012

© Springer-Verlag 2012

R. M. Pollyea (✉) · J. P. Fairley
Department of Geological Sciences,
University of Idaho, PO Box 443022,
Moscow, ID 83844-3022, USA
e-mail: rpollyea@vandals.uidaho.edu
Tel.: +1-208-8856192
Fax: +1-208-8855724

consequence of this paradox is that successful CO₂ sequestration in fractured basalt formations will largely depend on understanding how reservoir-scale heterogeneity impacts formation injectivity and confinement over the required time scales.

To date, much of the research directed toward understanding geologic CO₂ sequestration in fractured basalts has focused on the Columbia River Basalt Group (CRBG), which is a regionally expansive flood basalt complex covering the greater portions of eastern Washington, Oregon (USA), and, to a lesser extent, northwest Idaho. One series of numerical CO₂ injection simulations considering a relatively small injection rate and time scale (14–30 days and 12,000–26,000 tons CO₂/year, respectively) suggests adequate injectivity and confinement for a small-scale pilot study in the Umanum and Slack Canyon units of the CRBG at Wallula, Washington (McGrail et al. 2009). Although these results do not address the likelihood of success for commercial-scale CO₂ sequestration in basalt formations, they are encouraging nonetheless and serve to further motivate investigations of CO₂ sequestration at larger scales and within different basalt-rich geographic regions.

One such region is the east Snake River Plain (ESRP) in southern Idaho (Fig. 1), which has been proposed as an attractive basalt-hosted hydrogeologic system for CO₂ disposal. The favorable constitution of ESRP basalts is based largely on their mineral composition, which suggests an elevated reactive potential for permanent mineral trapping (Litynski et al. 2006). Recent estimates,

based on geographical information system (GIS) mapping and laboratory-derived porosity data, indicate that the storage capacity of the deep ESRP aquifer may be as high as 34 gigatons of CO₂ (Staires 2008). This indicates that the ESRP satisfies one of the three primary criteria (capacity) for reservoir suitability; however, the questions of injectivity and confinement remain open.

In this paper, a two-dimensional numerical modeling experiment of geologic carbon sequestration in ESRP basalts is performed to investigate injectivity and confinement potential at a commercially relevant reservoir scale and CO₂ injection rate. This model incorporates a field-based approach for reservoir characterization and focuses on the uncertainty associated with incomplete knowledge of individual basalt-flow distributions at target injection depths (below 800 m). This uncertainty is addressed by stochastic reservoir simulation and Monte Carlo-type CO₂ injection modeling using 100 equally probable heterogeneous reservoir domains. In addition to evaluating the injectivity and confinement potential of low-volume basalts, this work addresses several challenges encountered in most regional-scale hydrogeologic models (e.g., field sampling, anisotropic and depth dependent permeability structures, and reservoir uncertainty). In addressing these challenges, a suite of theoretical tools was applied with the intention that the application of these techniques may provide guidance for future investigations of this type.

Site description and conceptual model

The ESRP is a layered assemblage of low-volume vesicular basalt flows with an aggregate thickness between 1,000 and 2,000 m across much of the province's extent (Staires 2008). Individual ESRP basalt flow dimensions have been characterized by median length to width-to-thickness aspect ratio of 30:10:1 and length scale on the order of tens of meters to a kilometer (Welhan et al. 1997, 2002b). Internal flow morphology can be classified into four distinct features: (1) upper vesicular zone, (2) massive flow interior, (3) lower vesicular zone, and (4) lateral flow contacts consisting primarily of basalt rubble (Welhan et al. 2002c). Although this classification is adequate, the authors also refer to the traditional basalt flow description of upper and lower colonnades, of which the upper and lower vesicular zones are features within their respective colonnades. The term “interflow zone” has also been used to describe high permeability pathways composed of interconnected, densely fractured upper vesicular zones and rubbly lateral flow margins (Clemo and Welhan 2000; Welhan et al. 2002a, b, c).

Within the flow colonnades, ESRP basalts exhibit a columnar joint structure with column bounding (vertical) and column normal (horizontal) fractures being the most prevalent fracture types (Schaefer and Kattenhorn 2004). Fracture densities are greatest in the upper and lateral portions of the basalt flows where convective heat transfer to the atmosphere resulted in elevated thermal gradients

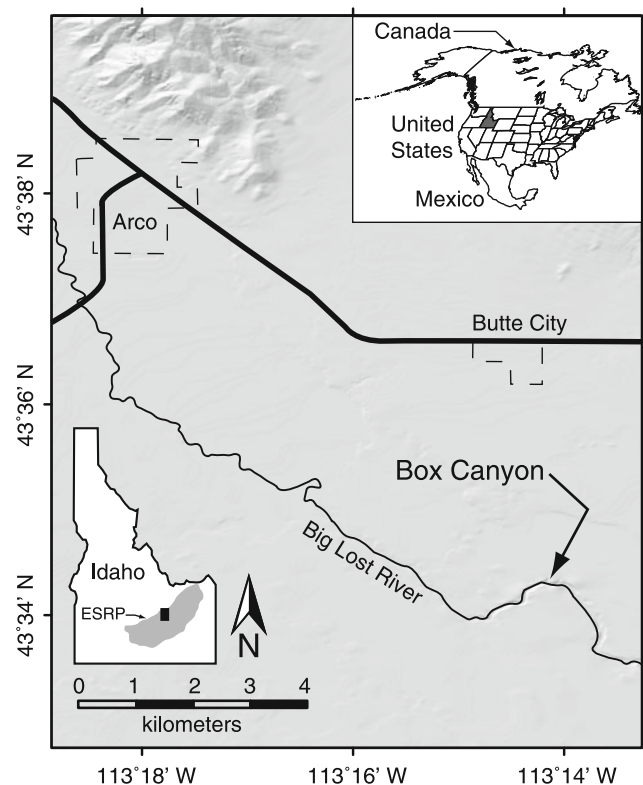


Fig. 1 Site location map for Box Canyon field site and east Snake River Plain (ESRP)

during emplacement (Lore et al. 2001; Schaefer and Kattenhorn 2004). Column bounding fractures, observed in plan view, define the edges of a polygonal network of columns that, in the upper colonnade, are cross-cut by column normal fractures, see, e.g. Fig. 3 in Lore et al. (2001). In order to represent this complex flow geometry at reservoir (kilometer) scale and maintain the computational efficiency required for Monte Carlo-type simulation runs, this system is modeled as a bimodal heterogeneous stochastic continuum. In this conceptual model, the structural characteristics of individual flow units are reduced to (1) densely fractured and rubble zones and (2) flow interiors (Fig. 2), where the rubble zones are known to exhibit much larger porosity and orders of magnitude greater permeability than the flow interiors (Doughty 2000).

Field sampling and semivariogram analysis

The stochastic continuum model for fractured rock implicitly invokes the equivalent porous media assumption (Long et al. 1982), which, for a heterogeneous reservoir model, is represented by spatially distributed subdomains (continua). These subdomains effectively aggregate the scale-dependent properties within each continuum and are later (see section [Reservoir simulation](#)) assigned characteristic properties, e.g. effective permeability, for flow and transport modeling. The spatial variability of each subdomain (continuum) in the conceptual model is quantified using the semivariogram measure of spatial correlation, which, for this application, requires data sufficient for two experimental semivariograms: (1) the semivariogram of permeable structures, i.e. fractures and rubble zone, across multiple flows, and (2) the semivariograms for permeable structures within each continuum. In both cases, field data are required with resolutions sufficient for identifying anisotropy within each continuum.

Field data suitable for flow-scale and continua-scale semivariogram analysis of ESRP permeability structures were acquired at the Box Canyon field site. The Box Canyon is an incised portion of the Big Lost River, located approximately 8km southeast of Acro, Idaho (Fig. 1), that permits access to vertical basalt exposures typical of the ESRP. The outcrop selected for this investigation is approximately 90m horizontal by 15m vertical, and offers cross-sectional exposures of two basalt

flows separated by a central rubbly flow margin (Fig. 2). The Box Canyon field sampling was performed in two campaigns, which are briefly described in the remainder of this section.

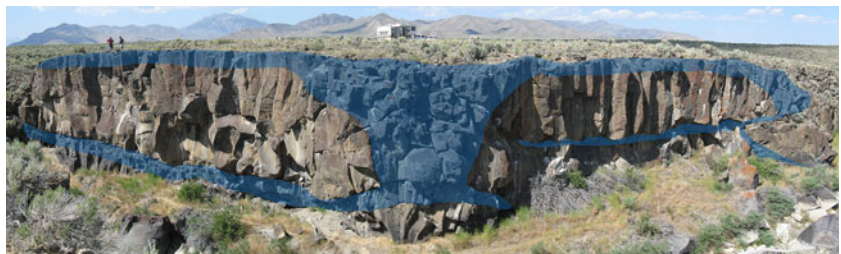
Field data for flow-scale semivariogram analysis of Box Canyon permeability structures were acquired in June 2010 using a Leica ScanStation2 terrestrial light detection and ranging (LiDAR) scanner. Fourteen individual scans were acquired and merged with a mean registration error of 0.004 m; the complete dataset contained ~65 million data points. These data were used to generate a binary fracture distribution map of the scanned exposure using a surface roughness model (Pollyea and Fairley 2011) with 0.125-m grid resolution (Fig. 3a). This fracture map is an expression of the bimodal conceptual model so that permeability structures (fracture and rubble) can be distinguished from the flow interior using the binary categorical transform:

$$i(\mathbf{u}) = \begin{cases} 1 & \text{fractured} \\ 0 & \text{otherwise} \end{cases} \quad (1)$$

where, i is the coded binary value at location \mathbf{u} . Semivariogram analysis of this binary fracture distribution was initiated using the semivariogram map (Deutsch and Journel 1998, varmap, pp. 55–57) and the results suggest the presence of anisotropic (direction dependent) fracture correlation along maximum and minimum axes of continuity approximately parallel to the horizontal and vertical outcrop dimensions, respectively (Fig. 3b). These directional orientations were used to calculate an anisotropic experimental semivariogram at 0.5-m lag intervals (Deutsch and Journel 1998, gamv, pp. 53–54); the experimental semivariogram was then modeled (Fig. 3c) according to the parameters in Table 1.

Field data for semivariogram analysis of each subdomain were obtained during a 2-week sampling campaign at the Box Canyon in June and July 2008. Spatially referenced data describing observed fractures and flow morphology were obtained from the outcrop by rappelling the canyon rim. Semivariograms for each subdomain (flow interior and rubble zone) were computed by segmenting the dataset into two subsets on the basis of flow morphology, i.e. data obtained within the entablature and upper or lower colonnades were assigned to the flow interior subdomain and data obtained within the rubble zones were assigned to the rubble subdomain. Spatial correlation of permeability structures was evaluated using the categorical transform (Eq. 1) and

Fig. 2 Digital image of Box Canyon outcrop illustrating bimodal conceptual model. The densely fractured upper colonnades and rubble zone are denoted with *blue shading*. *Unshaded* region represents flow interior



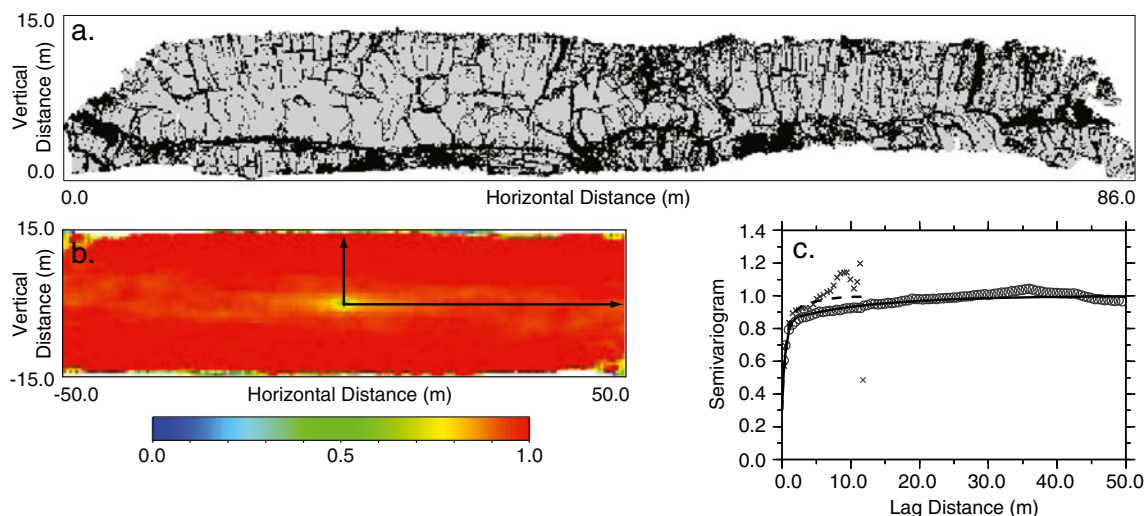


Fig. 3 Flow-scale geostatistical analysis of the Box Canyon outcrop. **a** Outcrop fracture map based on terrestrial LiDAR data; fractures are denoted with *black* and unfractured basalt denoted with *gray*. **b** Semivariogram map for fractures in **(a)**; *yellow and orange band spreading laterally* from the center suggests the axis of maximum spatial correlation. *Arrows* denote axes of maximum (horizontal) and minimum (vertical) spatial correlation. **c** Normalized experimental and model semivariograms for fractures in **(a)**. *Circles and x-symbols* denote horizontal and vertical experimental semivariograms, respectively. The *solid and dashed lines* denote horizontal and vertical model semivariograms, respectively. Model specifications are listed in Table 1

experimental and model semivariograms as described in the aforementioned. The flow interior subdomain was found to exhibit anisotropic spatial correlation with maximum and minimum axes of continuity in the same orientation as the flow-scale semivariogram (Fig. 4). Interestingly, the rubble-zone-experimental-semivariogram values were zero for all lags, which is the result of the rubble zone being pervasively fractured (i.e. every sample contained a fracture). While this suggests “perfect” correlation, the more meaningful implication is that fracture controlled transport parameters (i.e. permeability) in the rubble zone may be considered isotropic and homogeneous. This is discussed further in the following (section [Reservoir simulation](#)).

Reservoir simulation

Reservoir geometry is specified as a two-dimensional Cartesian grid with square 25-m gridblocks. The grid

dimensions are 5,000 m lateral and 1,000 m vertical (800–1,800 m depth), so the complete grid contains 8,000 blocks. Reservoir heterogeneity is incorporated using sequential indicator simulation, which is a non-Gaussian simulation algorithm that accounts for the areal proportion and spatial variability of each facies (in this case rubble zone or flow interior) using the probability distribution and model semivariogram, respectively. Sequential indicator simulation selects gridblocks in random order and (1) performs ordinary indicator kriging to establish the conditional probability that each simulated facies is present at the gridblock, and (2) assigns the gridblock a facies based on the conditional probability distribution (Deutsch 2002, p.196). For each simulated gridblock, the

Table 1 Model Semivariogram Parameters

	Model type	Sill	Range (m) ^a
Flow Scale			
Horizontal	Nugget effect	0.30	—
	Exponential	0.15	1.5
	Exponential	0.55	38
Vertical	Nugget effect	0.35	—
	Exponential	0.15	1.5
	Exponential	0.55	10
Flow Interior			
Horizontal	Nugget effect	0.4	—
	Exponential	0.4	3
	Exponential	0.2	20
Vertical	Nugget effect	0.4	—
	Exponential	0.4	3
	Exponential	0.2	5

^a m meters

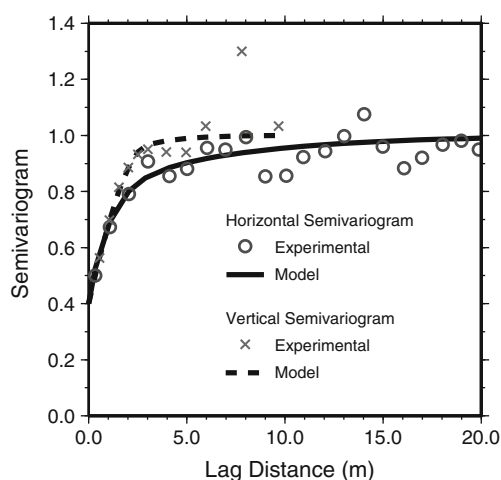


Fig. 4 Normalized experimental and model semivariograms for the flow interior subdomain. *Circles and x-symbols* denote horizontal and vertical experimental semivariogram values, respectively. *Solid and dashed lines* denote horizontal and vertical model semivariograms, respectively. Model specifications for the flow interior model semivariogram are listed in Table 1

indicator kriging routine conditions the probability distribution on both known data and previously simulated gridblocks so that the semivariogram and facies probability distribution are reproduced with some ergodic fluctuation (Goovaerts 1997, p 427). For the present work, fully unconditional simulations, i.e. maximum reservoir uncertainty, with the exception that the gridblock assigned to the injection well occurs in a rubble zone, were assumed. One hundred synthetic, heterogeneous reservoir models were computed for use with the Monte Carlo injection experiments presented in section [CO₂ injection model specification](#). To provide the reader with a sense for the spatial variability of these synthetic reservoirs models, three randomly selected examples are presented in Fig. 5.

The effective permeability for each subdomain (rubble zone and flow interior) was estimated using the self-consistent approach originally proposed by Dagan (1989, pp. 193–201) and revisited by Rubin (2003, pp. 128–132). The general idea underlying this technique is that a heterogeneous medium is homogenized so that both media are characterized by an a priori unknown effective permeability, k_{eff} . Perturbing the homogenized medium by the inclusion of some element with permeability k_i , selected randomly from the probability distribution of the heterogeneous medium, results in a pressure field that differs from that of the heterogeneous medium. However, the average pressure distribution across the homogenized media for the inclusion of all k_i , $i=1\dots n$, in the probability distribution results in equivalent pressure distributions for the two media (Rubin 2003, p. 128). Since k_{eff} is the

parameter that relates this phenomenon, the self-consistent approximation for m -dimensional isotropic effective permeability (k_{eff}) has the form:

$$k_{\text{eff}} = \frac{1}{m} \left[\int \frac{f_k(k)dk}{k + (m-1)k_{\text{eff}}} \right]^{-1} \quad (2)$$

where $f_k(k)$ is the probability distribution function corresponding to the heterogeneous inclusions with permeability, k (Rubin 2003, p. 129). For this isotropic effective permeability approximation, the heterogeneous inclusions are considered spherical elements; however, this technique has an auxiliary form that considers axis-symmetric elliptical inclusions allowing for the approximation of horizontal ($k_{\text{eff,h}}$) and vertical ($k_{\text{eff,v}}$) anisotropic effective permeability. The anisotropic self-consistent effective permeability approximation has the form:

$$k_{\text{eff,h}} = \frac{1}{2} \left[\int \frac{f_k(k)dk}{(k - k_{\text{eff,h}})\lambda(e) + 2k_{\text{eff,h}}} \right]^{-1} \quad (3)$$

$$k_{\text{eff,v}} = \left[\int \frac{f_k(k)dk}{k + \lambda(e)(k_{\text{eff,v}} - k)} \right]^{-1} \quad (4)$$

where $\lambda(e)$ is a scaling function (see Dagan 1989, Eq. 3.4.17, p. 192) and e is the ratio of vertical to horizontal

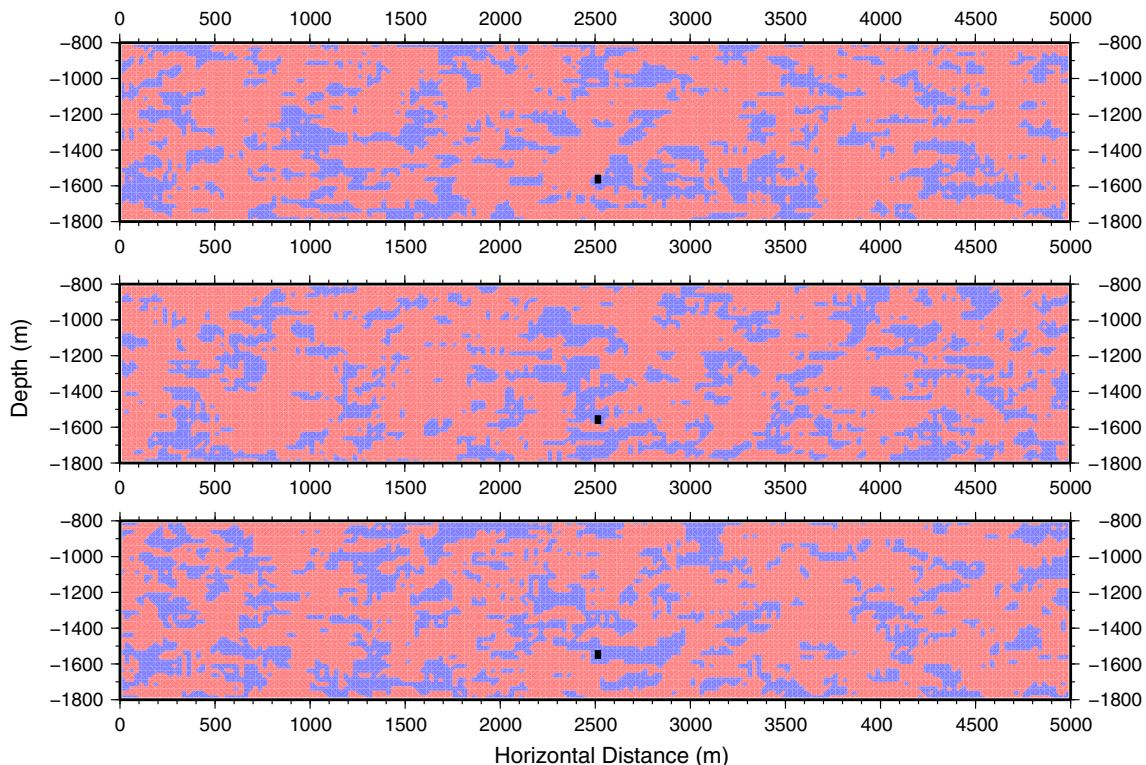


Fig. 5 A selection of three heterogeneous reservoir simulations. The flow interior subdomain is denoted with *pink shading*, the rubble zone subdomain is denoted with *purple shading*, and the injection sites are marked by *black squares*

anisotropy, which is specified in terms of covariance function integral scales for the effective medium (Dagan 1989, p. 198).

One challenge to the self-consistent technique is that sub-continuum-scale permeability data and the corresponding probability distribution $f_k(k)$ are needed for all permeability structures (inclusions) within each effective medium, which, for this investigation are defined as rubble zones or flow interiors (section [Site description and conceptual model](#)). This technique is data intensive; however, adequate data for estimating the effective permeability of each subdomain are available in the literature from a vadose zone investigation performed at the same Box Canyon outcrop on which the present study is based (Doughty 2000). In Doughty (2000), a two-dimensional section of the Box Canyon outcrop is discretized into $0.5 \text{ m} \times 0.5 \text{ m}$ square blocks, and each block is classified as massive basalt, vesicular basalt, a fracture type or rubble (Doughty 2000, plate 1) with corresponding horizontal and vertical permeability values provided (Doughty 2000, their Table 1). These data are applied to the present investigation by segmenting the dataset in two sections (0–10 m and 10–15 m depth), corresponding to the flow interior and rubble zone, respectively (Fig. 6) and the probability distributions for each section are obtained by simple box counting.

Applying the isotropic self-consistent method to the rubble zone subdomain is a straightforward application of the iterative solution to Eq. (2), which results in an effective permeability of $4.16 \times 10^{-10} \text{ m}^2$. In contrast, applying the anisotropic self-consistent model to the flow interior subdomain requires the additional step of

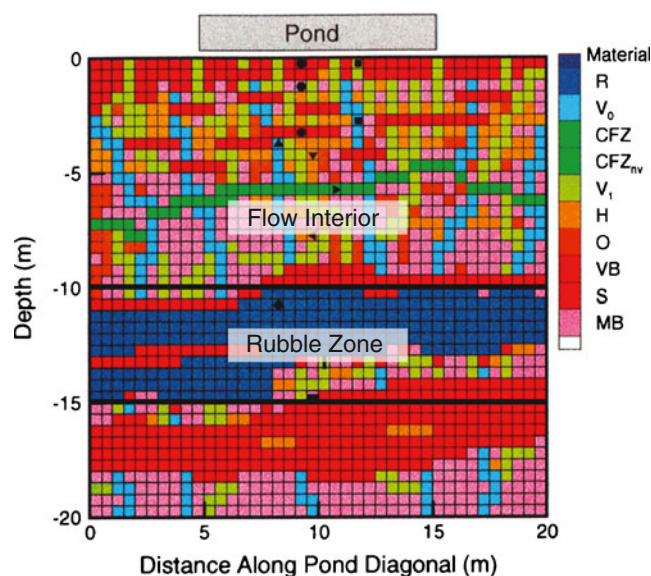


Fig. 6 Box Canyon map from Doughty (2000, plate 1; reproduced/modified by permission of American Geophysical Union). Lettered color codes denote material type: rubble (R), fractures (V_o , CFZ, V_i , H, O), basalt (VB, MB), soil (S). Horizontal and vertical permeability values for each material type are listed in Doughty (2000, their Table 1). For the present investigation, the data are segmented into two sections representing the bimodal conceptual model (flow interior and rubble zone) for use with the self-consistent effective permeability model

determining the horizontal to vertical anisotropy ratio—the e parameter in Eqs. (3) and (4). For this method, e is defined as the ratio of vertical to horizontal integral scales. These integral scales (I) are computed for each axis of spatial continuity using the relationship between the covariance function, $C(h)$, and semivariogram $\gamma(h)$, i.e. $I = \int_0^\infty C(h)dh = \int_0^\infty 1 - \gamma(h)dh$, where h is the lag distance. Using the vertical and horizontal semivariogram models presented in Fig. 4 (parameters are listed in Table 1), the vertical to horizontal anisotropy ratio is $0.78/1.73=0.45$. Incorporating this anisotropy ratio into the anisotropic self-consistent effective permeability technique results in vertical and horizontal effective permeabilities of 1.03×10^{-13} and $4.97 \times 10^{-13} \text{ m}^2$, respectively.

One limitation of these effective permeability estimates is that they are based on near-surface data, and are unlikely to represent the in situ permeability at depths of interest for CO_2 sequestration, which is typically deeper than 800 m (Orr 2009). For the present work, 800 m depth is assumed to be the upper boundary of a reservoir domain extending over a depth interval between 800 and 1,800 m. At these depths, formation permeability is influenced by lithostatic loading and natural mineral precipitation, both of which act to reduce formation permeability with increasing depth in the lithosphere. In accounting for these phenomena, a depth dependent permeability function, $k(z)$, is applied to the near-surface effective permeability estimates using the model proposed by Manning and Ingebritsen (1999) and extended to shallow depths ($\leq 800 \text{ m}$) by Saar and Manga (2004, Eqs. 39–40):

$$k(z) = \begin{cases} k_s e^{-z/\delta} & z \leq 800 \text{ m} \\ k_d \left(\frac{z}{d}\right)^{-3.2} & z > 800 \text{ m} \end{cases} \quad (5)$$

where, k_s is near surface permeability (i.e., the self-consistent effective permeability approximation for each continuum), δ is a fitting parameter, and k_d is the permeability at depth d , which for this model is 800 m. Effective permeability estimates for each continuum (rubble zones and flow interiors) are computed using Eq. (5), where the initial condition (k_s) corresponds with the self-consistent effective permeability approximation for each continuum (Fig. 7). The curves presented in Fig. 7 are conditioned on shallow borehole permeability data (Welhan et al. 2002a, Table 2) and the one available deep borehole data point (well INEL-1; Prestwich and Bowman 1980). Using these curves, the average effective permeabilities between 800–1,800 m depth are assigned to the flow interior ($k_{\text{eff},h}=3.40 \times 10^{-15} \text{ m}^2$ and $k_{\text{eff},v}=7.06 \times 10^{-16} \text{ m}^2$) and rubble zone ($k_{\text{eff}}=1.77 \times 10^{-14} \text{ m}^2$) for subsequent injection modeling.

CO₂ injection model specification

Carbon dioxide injection is simulated using TOUGH2-MP (Zhang et al. 2008) compiled with ECO2N, the equation of state module for mixtures of water, salt, and CO_2

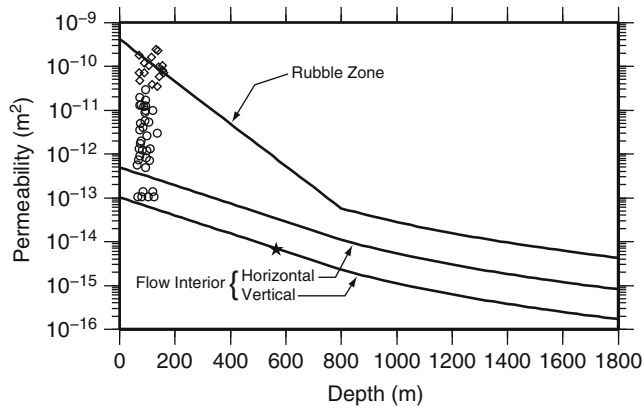


Fig. 7 Effective permeability as a function of depth using the permeability scaling models proposed by Manning and Ingebritsen (1999) and Saar and Manga (2004). Fitting parameters for each subdomain are: $\delta=210$ m (flow interior) and $\delta=90$ m (rubble zone). Borehole permeability data (Welhan et al. 2002a, Table 2) are plotted for wells intersecting “interflow” zone (diamonds) and wells that do not (circles). One deep data point is shown based on well drilling at INEL-1 (star) (Prestwich and Bowman 1980)

(Pruess 2005). Steady-state reservoir temperature and pressure conditions are computed by simulating non-isothermal groundwater flow in an initially fully saturated homogeneous reservoir domain bounded by a Dirichlet condition across the upper row of gridblocks ($T=32^{\circ}\text{C}$, $P=8$ MPa) and adiabatic (no flux) boundaries elsewhere. Additionally, a Neuman heat boundary with 0.11 W/m^2 is imposed at the bottom of the domain to account for the regional geothermal flux known from previous ESRP investigations (Brott et al. 1981). The resulting initial conditions are linear hydrostatic pressure and temperature distributions ranging from 8–17.5 MPa and 32–98 $^{\circ}\text{C}$, respectively. These conditions are representative of a saturated reservoir between 800–1,800 m below ground surface and are entirely within the supercritical temperature and pressure regime for CO_2 .

Boundary conditions for the CO_2 injection simulations are augmented to impose Dirichlet conditions at the lateral extent of the reservoir domain. As with most CO_2 sequestration models, this work suffers from insufficient site data to describe two-phase flow properties for the aqueous

phase and supercritical phase CO_2 . In keeping with similar studies by previous investigators (see e.g., Doughty and Pruess 2004), relative permeability is modeled using generic characteristic curves: van Genuchten (1980) for the aqueous phase and Corey (1954) for the supercritical CO_2 phase. For the same reason, capillary pressure effects resulting from interfacial tension between non-wetting supercritical CO_2 and the aqueous phase are accounted for using the generic van Genuchten (1980) capillary pressure model.

One hundred individual carbon injection simulations are performed using the bimodal heterogeneous property distributions described in section Reservoir simulation. The injection well is specified at the gridblock with nodal center corresponding to the approximate horizontal mid-point of the reservoir ($x=2,512.5$ m) and a depth of 1,562.5 m below ground surface. Supercritical CO_2 is injected into the system for 10 years at a constant mass rate of 21.6 kg/s (~680,000 metric tons per year), which represents half the annual CO_2 emissions generated by a typical 1,000 MW gas-fired power plant (Doughty and Pruess 2004).

Discussion

The results for 100 individual CO_2 injection simulations indicate the potential for two distinct outcomes: (1) a given simulation may complete the specified 10-year simulation time or (2) the simulation terminates within the first year of CO_2 injection (Fig. 8a). In the latter case, the simulations terminate because CO_2 injection generates excessive pressure accumulation near the injection site. Since each of the 100 reservoir models are identically parameterized and the injection well is consistently located within a high permeability rubble zone, the occurrence of excessive injection pressure accumulation suggests that spatially variable reservoir heterogeneity governs the rate and magnitude of pressure accumulation. Understanding the physical mechanisms controlling this behavior are an important criteria for evaluating formation injectivity.

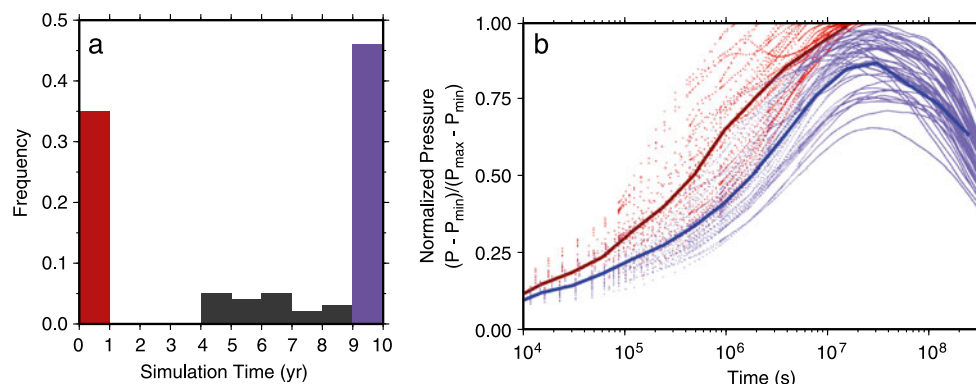


Fig. 8 Success rate data from numerical simulations. Maximum simulation time is 10 years. **a** Histogram of simulation time for 100 CO_2 injection runs; red and blue bars correspond to time series data in **(b)**. **b** Normalized injection block time-series pressure data for each CO_2 injection simulation for each time step (points) and the arithmetic mean for successful (blue) and unsuccessful (red) simulations

Insights about rate of injection pressure accumulation can be drawn from time-series pressure data recorded at the injection block for each time step for each individual simulation (Fig. 8b). The data are normalized because numerical values of pressures in a two-dimensional model may not be representative of the pressures that would be observed in a three-dimensional domain for a similar injection scenario; however, despite this limitation, the relationships found in the data are physically realistic and provide important information regarding the implications of reservoir uncertainty. In Fig. 8b, solid red and blue lines represent the arithmetic mean pressure for prematurely terminated and successful runs, respectively. Despite minor overlap in the raw data (Fig. 8b, points), the lesser rate of pressure accumulation for the successful runs (Fig. 8b, blue line) suggests that rubble zone connectivity near the point of injection more rapidly redistributes injection pressure.

The length scale of rubble zone connectivity necessary to effectively redistribute injection pressure into the surrounding formation is considered by evaluating the supercritical phase CO₂ saturation variance for the successful runs. The supercritical CO₂ saturation variance is computed for each gridblock at the final time step corresponding to 10 years of injection (Fig. 9a). In Fig. 9a, there are two distinct regions of elevated CO₂ saturation variance (plotted in red). The concentric pattern of elevated CO₂ saturation variance between 100 and 150 m from the injection block ($x=25, 12.5$ m, $z = -1,562.5$ m) indicates highly variable CO₂ migration routes for transport away from the injection block. This implies that, for any one simulation, discrete flow paths are energetically favorable for CO₂ migration and injection pressure redistribution at the 100–150-m-length scale due to advection dominated transport. Although the two-dimensional simulations presented here may not adequately represent the physical magnitude of this length scale, its presence in these simulations suggests a spatial threshold beyond

which dispersion significantly contributes to the transport process. This process is described physically by the initial formation of discrete, preferential flow paths within high permeability rubble zones near the injection site, and, over time, these flow paths are reinforced by a relative permeability feedback cycle that effectively isolates the flow path from the surrounding formation. Once initiated, this feedback process becomes a self-reinforcing system, whereby elevated CO₂ saturation increases the supercritical CO₂ phase permeability, which allows greater CO₂ entry; this process forms a feedback loop that continues until the maximum gas-phase relative permeability is achieved. As the feedback system becomes established, a “pipeline” is formed that provides the primary conduit for transport. This implies that formation injectivity sufficient for long-term CO₂ sequestration in low-volume basalt requires rubble zone connectivity to the surrounding aquifer on a length scale that is dependent on formation properties (e.g., permeability) and CO₂ injection rates. At this length scale away from the injection block, sufficient high permeability rubble zones exist to effectively redistribute injection pressure ahead of the advancing CO₂ plume. When sufficient rubble zone connectivity exists at this length scale, the combined effects of advection and dispersion act in concert to redistribute injection pressure farther into the reservoir which, combined with the established near-borehole high-permeability pathway, result in a pressure drop near the injection point. This effect is illustrated in Fig. 8b, where the injection block pressures for the successful runs (Fig. 8b, blue data) drop after $\sim 3 \times 10^7$ s (347 days).

Insight into the confinement potential for low-volume ESRP basalts is considered by evaluating the expected value for supercritical phase CO₂ distribution over each of the 46 successful simulations. The expected value (mean or e-type estimate) is computed at each gridblock for the final time step, which corresponds to 10 years of constant rate injection (Fig. 9b). After 10 years, the CO₂ plume has

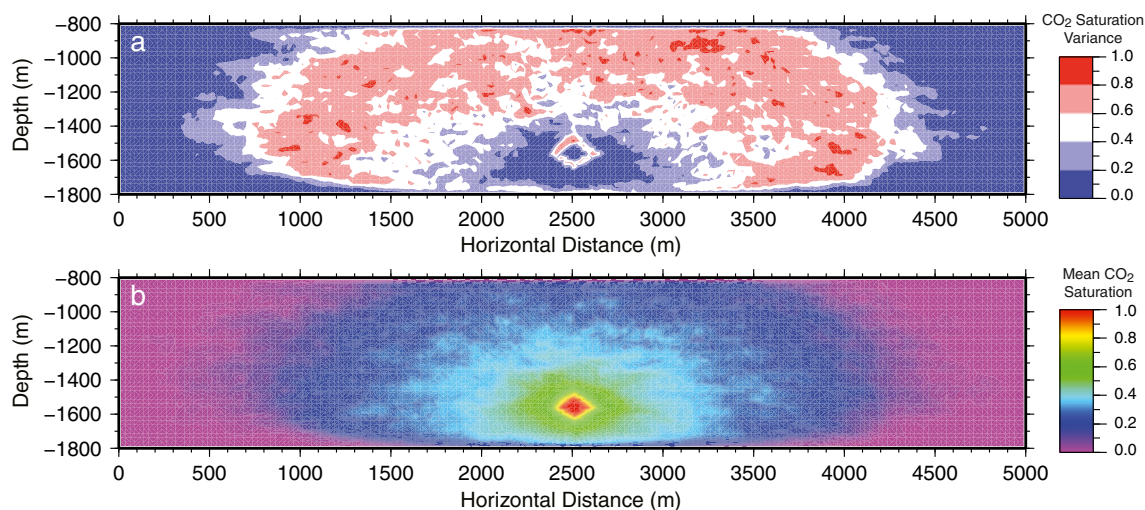


Fig. 9 Aggregate results for the 46 successful CO₂ injection simulations. **a** Normalized variance contours of supercritical CO₂ saturation; note the concentric region of elevated uncertainty within ~ 150 m around the injection block. This suggests heterogeneous control of preferential CO₂ migration away from the injection site. **b** Contours of mean supercritical CO₂ saturation

a maximum lateral extent of ~2,000 m from the injection block, suggesting that lateral plume migration may support a level of physical trapping. However, the extensive distribution of non-zero mean supercritical CO₂ saturations across the upper reservoir domain indicates that density driven upward CO₂ migration exceeds the reservoir capacity for physical trapping (by capillary forces or residual saturations) over the 10-year simulation interval. Similarly, the variance of supercritical CO₂ saturation (Fig. 9a) indicates that CO₂ saturation at the upper boundary is highly variable, and suggests that CO₂ is escaping through the upper model boundary by discrete flow paths. The occurrence and spatial variability of discrete flow paths for vertical transport also suggests a complicating factor for siting well networks to monitor for this escape. To give the reader a sense for the temporal evolution of the supercritical phase CO₂ plume, the time series plot for a single simulation is presented in Fig. 10. Although the simulation presented in Fig. 10 is only one of the 46 successful (i.e. 10 year) runs, the result suggests that supercritical phase CO₂ reaches the upper boundary by ~5 years of injection. The temporal threshold at which this boundary is reached is an important criterion for

evaluating confinement potential because the upper boundary is specified at 32°C and 8 MPa, which is very close to the lower temperature and pressure limits for supercritical phase CO₂. As supercritical CO₂ migrates above 800 m it will undergo phase change from supercritical to gas phase, resulting in significantly lower density and greater buoyancy, thus enhancing the potential for escape.

While the vertical migration of CO₂ demonstrated here may suggest that low-volume basalt formations exhibit insufficient confinement potential for long-term CO₂ disposal, the authors propose that these simulations are indicative of a worst case scenario. In particular, several investigators have noted thin lenses (meter scale) of fine-grained sedimentary units interbedded within core samples of ESRP basalts (Welhan and Reed 1997; Magnuson 2004); however, the areal extent and continuity of these features is largely unknown. Upon inspection of exposures at Box Canyon and Malad Gorge (a similar exposure to Box Canyon with ~60 m vertical relief), sedimentary interbeds were not present at sufficient thickness to obtain meaningful correlation statistics. For this reason, they are omitted from the conceptual model considered here. If

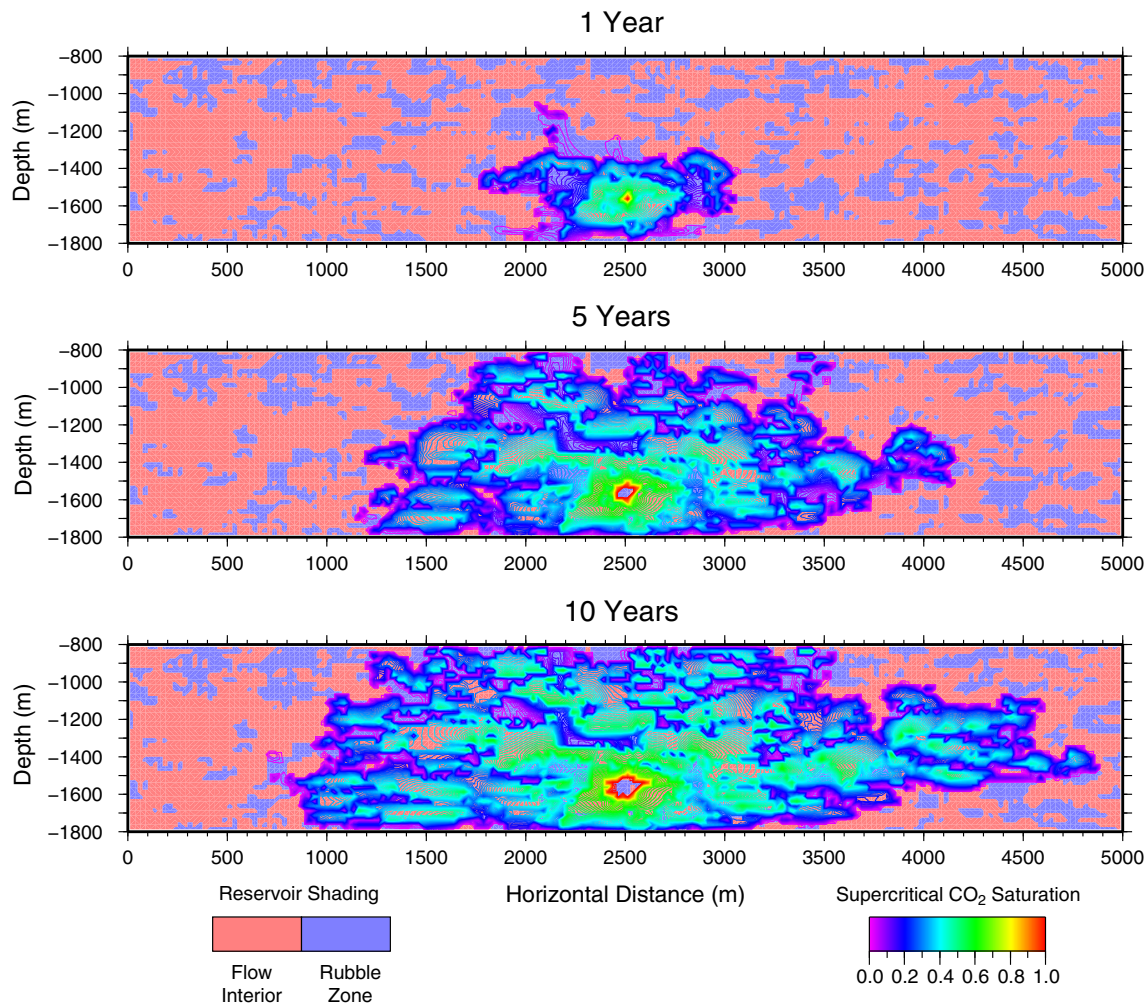


Fig. 10 Time lapse supercritical CO₂ saturation for a single injection simulation. Note that by 5 years simulation time, supercritical phase CO₂ has reached the upper boundary via three discrete migration routes

these features are found with sufficient areal extent for inhibiting the discrete escape routes suggested by Fig. 9a, they would represent important physical barriers that enhance formation confinement. Another factor contributing to the conservative nature of these simulations is that mineral precipitation is not considered; however, this process must be expected to play an important role in any long-term geologic sequestration scenario. For example, mineral precipitation may preferentially reduce high permeability structures because these features receive greater CO₂ mass, and therefore, would be subject to greater precipitation rates. Mineralization at a sufficiently high rate may regulate the effective permeability of the overall system toward some equilibrium between the upper and lower limits. In depleted petroleum reservoirs and other sedimentary sequestration reservoirs, CO₂ mineralization is generally thought to be kinetically inhibited; however, one of the advantages of basalt formations is their hypothesized ability to quickly mineralize free CO₂ (McGrail et al. 2006). If this potential exists, then the results presented here suggest that mineralization rates sufficient for measureable permeability reduction may be required within the first 5 years of injection.

Conclusions

In this paper a Monte Carlo-type numerical modeling experiment of geologic carbon sequestration into 100 fractured, low-volume basalt hosted aquifers with characteristics typical of the east Snake River Plain, Idaho was performed. The model presented here, while not specific to an individual project, provides insights into formation injectivity and confinement potential for geologic carbon sequestration in low-volume basalts at a commercially relevant reservoir scale and injection rate. One result of this experiment suggests that the spatial distribution of heterogeneous permeability structures exerts significant influence on formation injectivity. In particular, the model presented here demonstrates that the spatial distribution of high permeability rubble zones and the connectivity length of these units from the injection well into the target reservoir is a primary factor influencing the rate of injection pressure accumulation within the first year of injection. The implication of this result is that a successful field implementation of CO₂ sequestration in fractured, low-volume basalt formations will depend, to a large extent, on the ability to demonstrate good permeability and connectivity for a high permeability zone. Moreover, if the target injection rates are known a priori and reasonable estimates of formation permeability can be obtained, then this connectivity length scale can be estimated by numerical simulation in three dimensions and tested in the field using short term injection testing.

The evaluation of reservoir confinement with respect to the spatial distribution of heterogeneous permeability structures was less conclusive. The analysis of mean supercritical CO₂ saturations for the 46 successful

simulations suggests that physical trapping alone may be insufficient to prevent escape by vertical migration, at least within the conservative assumptions of the model presented here. Alternatively, the potential that areally extensive, low-permeability sedimentary interbeds occur within the ESRP suggests that the simulations represent a worst-case scenario. Additionally, the model presented here does not include the effects of mineralization, which may act to increase reservoir confinement. Ultimately, the question of reservoir confinement in fractured basalts will require a great deal of continued research to understand the coupled processes required for numerical simulation and to establish constraints on in situ mineralization rates.

In addition to the model results and conclusions presented here, a series of theoretical techniques is combined to demonstrate a field-based approach for reservoir characterization and parameterization. These techniques include the combined applications of outcrop fracture mapping with terrestrial LiDAR data (Pollyea and Fairley 2011), implementing the self-consistent effective permeability models (Dagan 1989; Rubin 2003), and accounting for the depth dependence of permeability using near surface data (Manning and Ingebritsen 1999; Saar and Manga 2004). It is the authors' hope that demonstrating the application of these methods, in a comprehensive manner, may provide useful guidance for future investigations of this type.

Acknowledgements The authors thank Robert Podgorney for his assistance with TOUGH2-MP. Jennifer Hinds provided assistance in preparing figures; her efforts are appreciated. This work was greatly improved by the challenging comments from three anonymous reviewers. Financial support has been provided by the Center for Advanced Energy Studies under contract number DE-AC07-05ID14517.

References

- Bachu S (2008) CO₂ storage in geological media: role, means, status and barriers to deployment. *Prog Energy Combust Sci* 34:254–273
- Brott CA, Blackwell DD, Ziagos JP (1981) Thermal and tectonic implications of heat flow in the east Snake River Plain, Idaho. *J Geophys Res* 86:11709–11734
- Clemon T, Welhan J (2000) Simulating basalt lava flows using a structure imitation approach. In: *Proc. of the Computational Methods in Water Resources XIII*, Alberta CA, June 2000, pp 841–848
- Corey A (1954) The interrelation between gas and oil relative permeabilities. *Producers Monthly* 19(1):38–41
- Dagan G (1989) *Flow and transport in porous formations*. Springer, Berlin
- Deutsch CV (2002) *Geostatistical reservoir modeling*. Oxford University Press, New York
- Deutsch CV, Journel AG (1998) *GSLIB: Geostatistical software library and user's guide*, 2nd edn. Oxford University Press, New York
- Doughty C (2000) Numerical model of water flow in a fractured basalt vadose zone: Box Canyon site, Idaho. *Water Resour Res* 36(12):3521–3534
- Doughty C, Pruess K (2004) Modeling supercritical carbon dioxide injection in heterogeneous porous media. *Vadose Zone J* 3:837–847

- Goovaerts P (1997) *Geostatistics for natural resource evaluation*. Oxford University Press, New York
- Jayaraman K (2007) India's carbon dioxide trap. *Nature* 445:350
- Litynski JT, Klara SM, McIlvried HG, Srivastava RD (2006) The United States Department of Energy's Regional Carbon Sequestration Partnerships program: a collaborative approach to carbon management. *Environ Int* 32:128–144
- Long J, Remer J, Wilson C, Witherspoon P (1982) Porous media equivalents for networks of discontinuous fractures. *Water Resour Res* 18(3):645–658
- Lore J, Aydin A, Goodson K (2001) A deterministic methodology for prediction of fracture distribution in basaltic flows. *J Geophys Res* 106(B4):6447–6489
- Magnuson S (2004) Regulatory modeling for the Idaho National Engineering and Environmental Laboratory's subsurface disposal area and conceptual model uncertainty treatment. *Vadose Zone J* 3:59–74
- Manning C, Ingebritsen S (1999) Permeability of the continental crust: Implications of geothermal data and metamorphic analysis. *Rev Geophys* 37:127–150
- Matter JM, Kelemen PB (2009) Permanent storage of carbon dioxide in geological reservoirs by mineral carbonation. *Nat Geosci* 2:837–841. doi:10.1038/NGEO683
- McGrail BP, Schaef HT, Ho AM, Chien Y-J, Dooley JJ (2006) Potential for carbon dioxide sequestration in flood basalts. *J Geophys Res* 111. doi:10.1029/2005JB004169
- McGrail B, Sullivan E, Spane F, Bacon D, Hund G, Thorne P, Thompson C, Reidel S, Colwell F (2009) Preliminary hydrogeologic characterization results from the Wallula Basalt Pilot Study. Technical report, December 2009, National Energy Technology Laboratory, Morgantown, WV
- Orr FM Jr (2009) Perspective: onshore geologic storage of CO₂. *Science* 325:1656–1657
- Pollyea RM, Fairley JP (2011) Estimating surface roughness of terrestrial laser scan data using orthogonal distance regression. *Geology* 39(7):623–626. doi:10.1130/G32078.1
- Prasad P, Sarma DS, Sudhakar L, Basavaraju U, Singh RS, Begum Z, Archana K, Chavan C, Charan S (2009) Geological sequestration of carbon dioxide in Deccan basalts: preliminary laboratory study. *Curr Sci* 96(2):288–291
- Prestwich S, Bowman J (1980) Completion and testing report: INEL geothermal exploratory well one (INEL-1). Technical report IDO-10096, US Department of Energy, Washington, DC
- Pruess K (2005) ECO2N: a TOUGH2 fluid property module for mixtures of water, NaCl, and CO₂. Technical report LBNL-57952, Lawrence Berkeley National Laboratory, Berkeley, CA
- Rubin Y (2003) *Applied stochastic hydrology*. Oxford University Press, New York
- Saar M, Manga M (2004) Depth dependence of permeability in the Oregon Cascades inferred from hydrogeologic, thermal, seismic, and magmatic modeling constraints. *J Geophys Res* 109. doi:10.1029/2003JB002855
- Schaef TH, McGrail PB (2009) Dissolution of Columbia River Basalt under mildly acidic conditions as a function of temperature: experimental results relevant to the geological sequestration of carbon dioxide. *Appl Geochem* 24:980–987
- Schaefer CJ, Kattenhorn SA (2004) Characterization and evolution of fractures in low-volume pahoehoe lava flows, eastern Snake River Plain, Idaho. *Geol Soc Am Bull* 116(3/4):322–336
- Staires DA (2008) Assessing the viability of carbon dioxide sequestration in Eastern Snake River Plain basalts, southern Idaho. MSc Thesis, Idaho State University, USA
- Van Genuchten M (1980) A closed-form equation for predicting the hydraulic conductivity of unsaturated soils. *Soil Sci Soc Am* 44:892–898
- Welhan JA, Reed MF (1997) Geostatistical analysis of regional hydraulic conductivity variations in the Snake River Plain aquifer, eastern Idaho. *Geol Soc Am Bull* 109(7):855–868
- Welhan J, Smith R, Wylie A (1997) Stochastic modeling of hydraulic conductivity in the Snake River Plain aquifer: 1. hydrogeologic constraints and conceptual approach. In: *Proceedings of the 32nd Engineering Geology and Geotechnical Engineering Symposium*, Boise, ID, March 1997, pp 75–91
- Welhan JA, Clemo TM, G go EL (2002a) Stochastic simulation of aquifer heterogeneity in a layered basalt aquifer system, eastern Snake River Plain, Idaho. In: Link PK, Mink L (eds) *Geology, hydrogeology, and environmental remediation: Idaho National Engineering and Environmental Laboratory, Eastern Snake River Plain, Idaho*. *Geol Soc Am Spec Pap* 353, pp 225–247
- Welhan JA, Johannesen CA, Davis LL, Reeves KS, Glover JA (2002b) Overview and synthesis of lithologic controls on aquifer heterogeneity in the eastern Snake River Plain, Idaho. In: Bonnichsen B, White C, McCurry M (eds) *Tectonic and magmatic evolution of the Snake River Plain Volcanic Province*. *Bull Idaho Geol Surv* 30:455–460
- Welhan JA, Johannesen CM, Reeves KS, Clemo TM, Glover JA, Bosworth KW (2002c) Morphology of inflated pahoehoe lavas and spatial architecture of their porous permeable zones, eastern Snake River Plain, Idaho. In: Link PK, Mink L (eds) *Geology, hydrogeology, and environmental remediation: Idaho National Engineering and Environmental Laboratory, eastern Snake River Plain, Idaho*. *Geol Soc Am Spec Pap* 353:135–150
- Zhang K, Wu Y-S, Pruess K (2008) User's guide for TOUGH2-MP: a massively parallel version of the TOUGH2 Code. Technical report LBNL-315E, Lawrence Berkeley National Laboratory, Berkeley, CA